Computer Methods and Programs in Biomedicine 244 (2024) 107975

Contents lists available at ScienceDirect

Computer Methods and Programs in Biomedicine

journal homepage: www.elsevier.com/locate/cmpb

# Constrained estimation of intracranial aneurysm surface deformation using 4D-CTA

Hujin Xie [a,b,*], Hao Wu [c], Jiaqiu Wang [a,b,d], Jessica Benitez Mendieta [a,b], Han Yu [a,b], Yuqiao Xiang [a,b], Haveena Anbananthan [a,b], Jianjian Zhang [e], Huilin Zhao [e], Zhengduo Zhu [a,b], Qiuxiang Huang [a,b], Runxing Fang [c], Chengcheng Zhu [f], Zhiyong Li [a,b,g,*]

[a] School of Mechanical, Medical and Process Engineering, Queensland University of Technology, Brisbane, QLD 4000, Australia
[b] Centre for Biomedical Technologies, Queensland University of Technology, Brisbane, QLD 4000, Australia
[c] School of Biological Science & Medical Engineering, Southeast University, Nanjing, Jiangsu 210096, China
[d] School of Engineering, London South Bank University, London, UK
[e] Department of Radiology, Ren Ji Hospital, Shanghai Jiao Tong University School of Medicine, 160 Pujian Road, Shanghai, China
[f] Department of Radiology, University of Washington School of Medicine, Seattle, WA, United States
[g] Faculty of Sports Science, Ningbo University, Ningbo, Zhejiang 315211, China

ARTICLE INFO

*Keywords:*
Biomechanical model
Intracranial aneurysms
4D-CTA
Data-driven
Constrained estimation

ABSTRACT

*Background and objective:* Intracranial aneurysms are relatively common life-threatening diseases, and assessing aneurysm rupture risk and identifying the associated risk factors is essential. Parameters such as the Oscillatory Shear Index, Pressure Loss Coefficient, and Wall Shear Stress are reliable indicators of intracranial aneurysm development and rupture risk, but aneurysm surface irregular pulsation has also received attention in aneurysm rupture risk assessment.

*Methods:* The present paper proposed a new approach to estimate aneurysm surface deformation. This method transforms the estimation of aneurysm surface deformation into a constrained optimization problem, which minimizes the error between the displacement estimated by the model and the sparse data point displacements from the four-dimensional CT angiography (4D-CTA) imaging data.

*Results:* The effect of the number of sparse data points on the results has been discussed in both simulation and experimental results, and it shows that the proposed method can accurately estimate the surface deformation of intracranial aneurysms when using sufficient sparse data points.

*Conclusions:* Due to a potential association between aneurysm rupture and surface irregular pulsation, the estimation of aneurysm surface deformation is needed. This paper proposed a method based on 4D-CTA imaging data, offering a novel solution for the estimation of intracranial aneurysm surface deformation.

## 1. Introduction

Intracranial aneurysms (IAs) are characterized by deterioration of the local structure of the arterial wall, loss of the internal elastic layer and interruption of the media, and it occurs in 3% to 5% of the general population, which is estimated to be 6 million people in the United States [1]. The annual rate of IAs rupture varies from 0.1% to 1.4%, according to relevant surveys [2,3]. Even though the overall rupture rate of IAs is relatively small, the rupture of IAs is a catastrophic event. The mortality rate of IAs rupture is 32% to 67%, and one-third of survivors have serious complications [4]. Therefore, the rupture risk assessment of IAs is a crucial consideration, and it is critical to examine and analyze aneurysms using patient-specific data.

Due to the significant health risks associated with aneurysm rupture, several risk factors have been well studied: age, family history, smoking, hypertension, and aneurysm size and location. These factors are used in aneurysm risk assessment and treatment strategies, such as the PHASES scoring system, which includes population, hypertension, age, size of the aneurysm, and early subarachnoid haemorrhage [5]. However, risk assessments based on these population-based data only achieve moderate accuracy. Although the treatment threshold is commonly 7 *mm*, many ruptured IAs are smaller than 7 *mm* [6]. Therefore, researchers have

* Corresponding authors at: School of Mechanical, Medical and Process Engineering, Queensland University of Technology, Brisbane, QLD 4000, Australia.
*E-mail addresses:* hujin.xie@hotmail.com (H. Xie), zylicam@gmail.com (Z. Li).

https://doi.org/10.1016/j.cmpb.2023.107975
Received 28 June 2023; Received in revised form 8 November 2023; Accepted 7 December 2023
Available online 10 December 2023

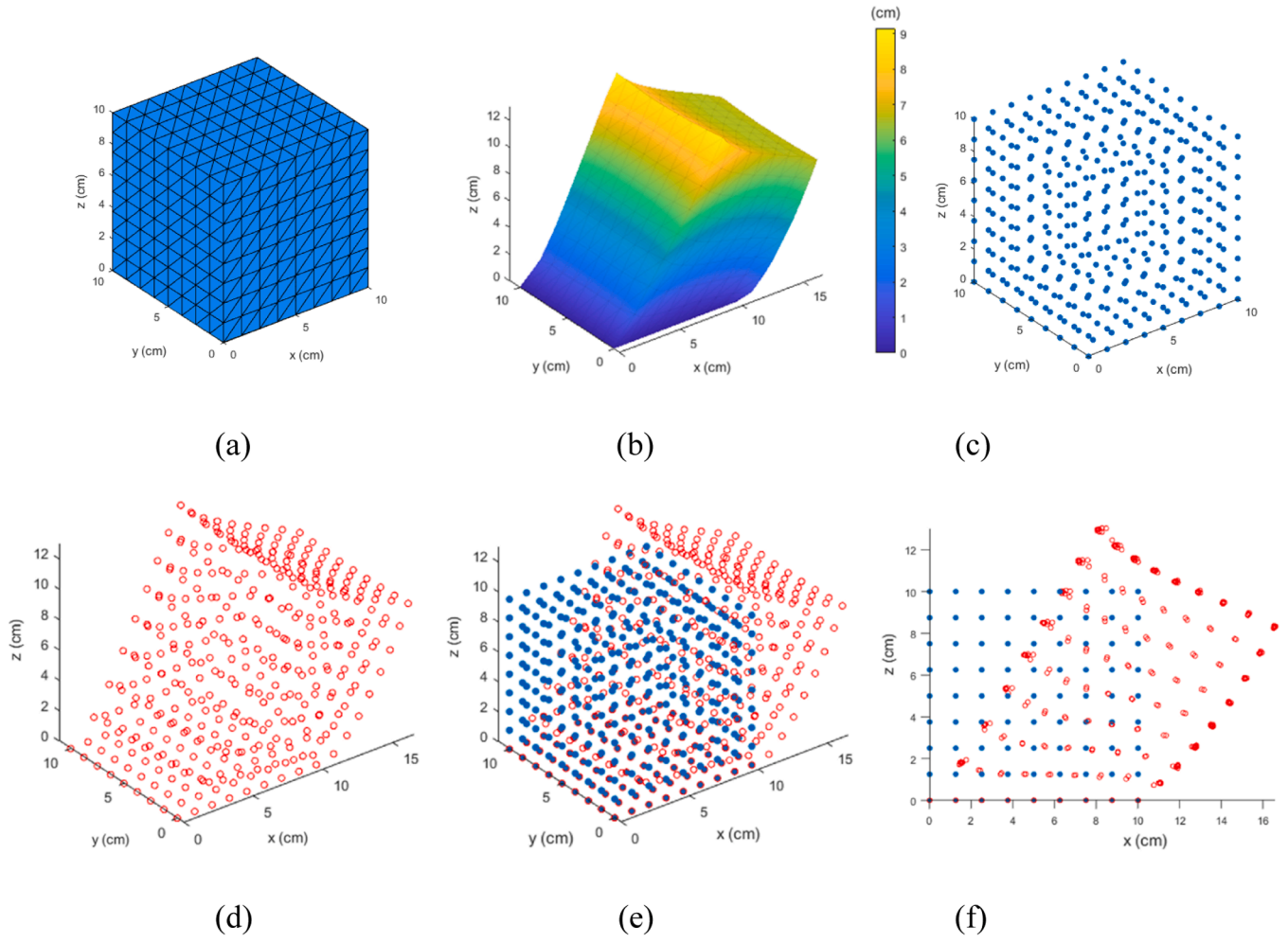


**Fig. 1.** The cubic model: (a) The original model; (b) FEA deformation result; (c) The original point cloud; (d) The deformed point cloud; (e) The contrast plot; (f) The front view of the contrast plot.

examined other quantifiable parameters and imaging information to allow for more patient-specific stratification of IA rupture risk.

Many research efforts have investigated the biomechanical parameters for IAs rupture risk assessment. Computational fluid dynamic (CFD) is a typical method to analyze patient-specific hemodynamic parameters [7,8]. These simulations consider factors such as the size and shape of the aneurysm, the velocity and pressure of the blood flow, and the properties of the blood itself [9]. It analyses the factors that are related to aneurysm growth and rupture, such as the Oscillatory Shear Index (OSI), Pressure Loss Coefficient (PLc) and Wall Shear Stress (WSS), which have been identified as an indicator of development and rupture risk for aneurysm [10,11]. It has been shown that the WSS within an IA is influenced by the geometry of the aneurysm, the velocity of the blood flow, and the pressure gradients within the aneurysm. These haemodynamic parameters have been shown to cause stress on the aneurysm wall, leading to deformation and growth over time. Among them, the WSS parameter has been of great interest, and these extensive studies demonstrated a correlation between WSS and aneurysm rupture [12–15].

Aneurysm wall thickness and mechanical properties have also received attention in aneurysm studies [16,17]; therefore, aneurysms have been studied using fluid-structure interaction (FSI), where the FSI analysis assumes that the vessel is deformable [18,19], and FSI can be realized using 1-way or 2-way couplings, and the FSI analysis results show that the equivalent strains were higher in ruptured aneurysms than unruptured aneurysms [20]. FSI has also been used in patient-specific models to study the risk of aneurysm rupture associated with traumatic brain injury (TBI) [21]. In addition to hemodynamic parameters, the aneurysm wall deformation has also received attention for aneurysm rupture risk assessment, and it has been shown that inhomogeneous mechanical features and abnormal wall motion are often associated with IAs symptoms, growth and rupture [22,23]. More in-depth studies have shown subjective parameters of irregular wall motion and deformation in growing or ruptured IA, such as irregular pulsation and pulsating haemorrhage. For example, a study has shown that intracranial aneurysms that exhibit irregular wall pulsation are more likely to rupture than those with regular wall pulsation [24]. In addition, the degree of irregular pulsation positively correlates with the risk of rupture [25].

As irregular pulsation of aneurysms may be a potential parameter for assessing the risk of rupture, some research efforts have focused on the estimation of aneurysm surface deformation. Since the deformation of the aneurysm is very small, any rigid motion must be fully compensated for to have an accurate estimate [26]. Due to the small deformation of IAs, optical flow (OF) methods are applied to image registration (IR) [27] because these methods are very suitable for recovering a small magnitude of displacement in the image [28]. However, OF methods are sensitive to intensity variations due to noise and inhomogeneity of contrast distribution and can lead to an unsmooth final deformation field [29]. Dynamic cardiac gated magnetic resonance angiography (MRA) and computed tomography angiography (CTA) have been used to estimate IAs wall motion with some success [30–32]. However, IA surface motion has proven difficult to quantify with conventional imaging

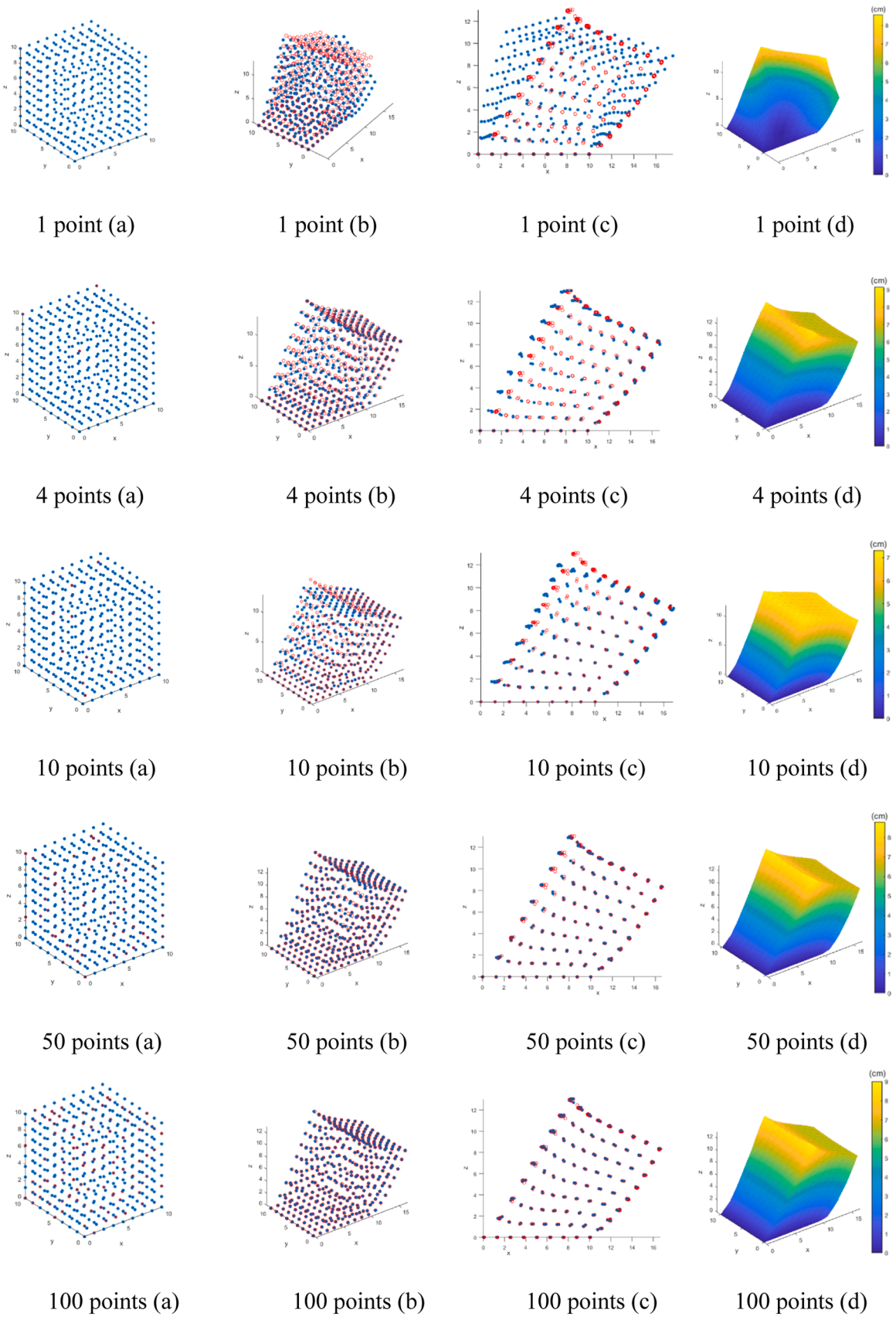


**Fig. 2.** The constrained estimated results by using the different number of sparse data points: (a) The sparse data points (red) on the surface; (b) The estimation result (blue) compares with the FEA result (red); (c) The front view of estimation result; (d) The colourmap of the estimation result.

**Table 1**
Statistical error analysis of constrained estimation by using different numbers of sparse data points.

| $N_{sprs}s$ | Mean Square Error | Mean Absolute Error | Root Mean Square Deviation |
|---|---|---|---|
| 1 | 2.2185 | 0.9920 | 1.4895 |
| 4 | 0.0539 | 0.1501 | 0.2322 |
| 10 | 0.0143 | 0.0658 | 0.1199 |
| 50 | 0.0028 | 0.0204 | 0.0530 |
| 100 | 0.0007 | 0.0095 | 0.0279 |

techniques due to the small size and limited spatial resolution of IAs. Three-dimensional reconstruction of aneurysms is critical for deformation estimation [33–35]. Some investigators recovered aneurysm pulsation by deforming the volume rendered by three-dimensional rotational angiography (3D-RA) and have compared the constructed volume projections to match the 2D image data set used for volume reconstruction [36]. However, this method has only been tested with phantom data and not validated using patient-specific data. Nowadays, 4D-CTA is becoming increasingly popular as a novel imaging technique in the evaluation of IAs. These scans provide a series of images of the aneurysm over time, allowing visualization of changes in size and shape. However, the identification of irregular pulsations is currently carried out through manual evaluation. In previous studies [23,37], three experienced neuroradiologists with 6 years of expertise in neurovascular CTA diagnosis independently assessed the presence of irregular pulsations while maintaining patient confidentiality and utilizing three-dimensional rotational angiographic images. In instances where a focal aneurysmal protuberance was identified within an aneurysm, the reviewers measured the maximum perpendicular height of this protuberance, deeming irregular pulsations present when at least three consecutive frames exhibited a focal aneurysmal protuberance ($\geq 1mm$). It's worth noting that this manual process may introduce discrepancies

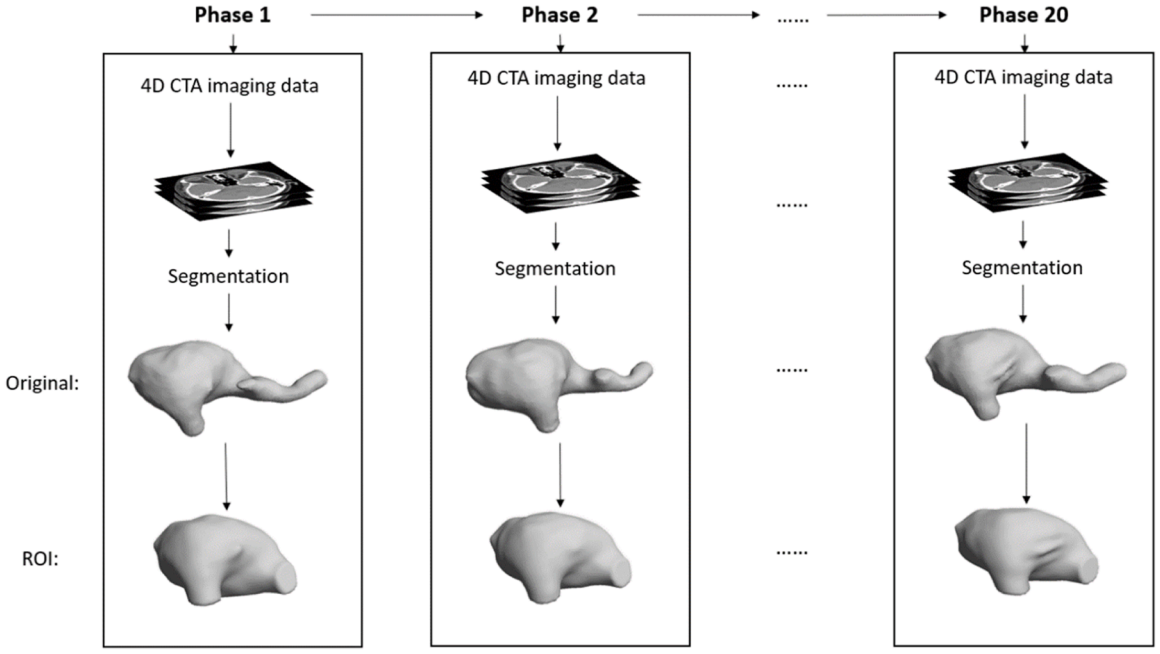


**Fig. 3.** Segmentation procedure for constructing patient-specific intracranial aneurysm 3D models using 4D-CTA imaging data.

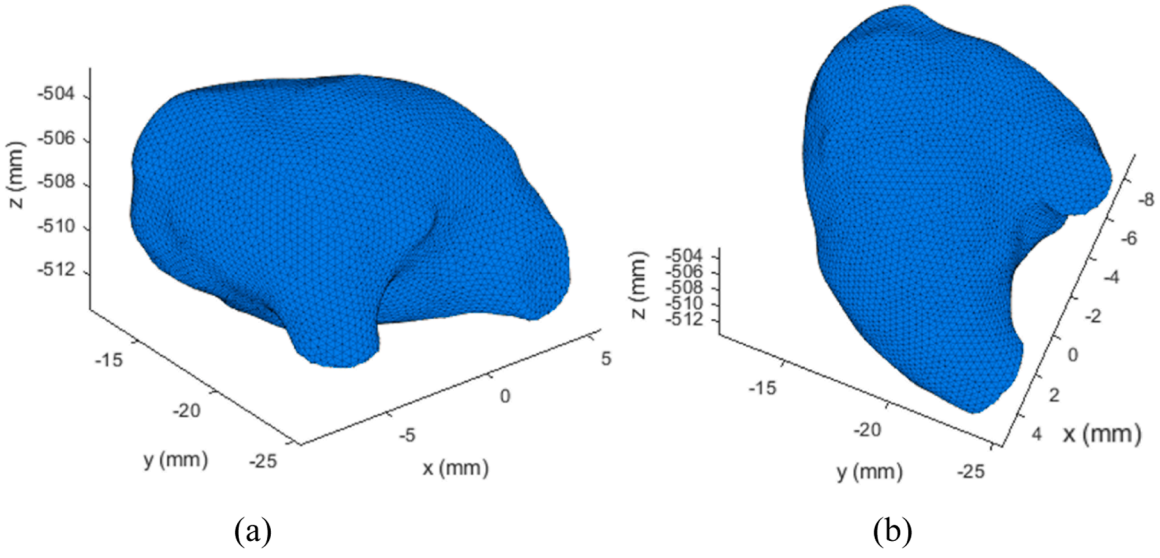


**Fig. 4.** The patient-specific intracranial aneurysm model with surface mesh in different angles of view at phase 1.

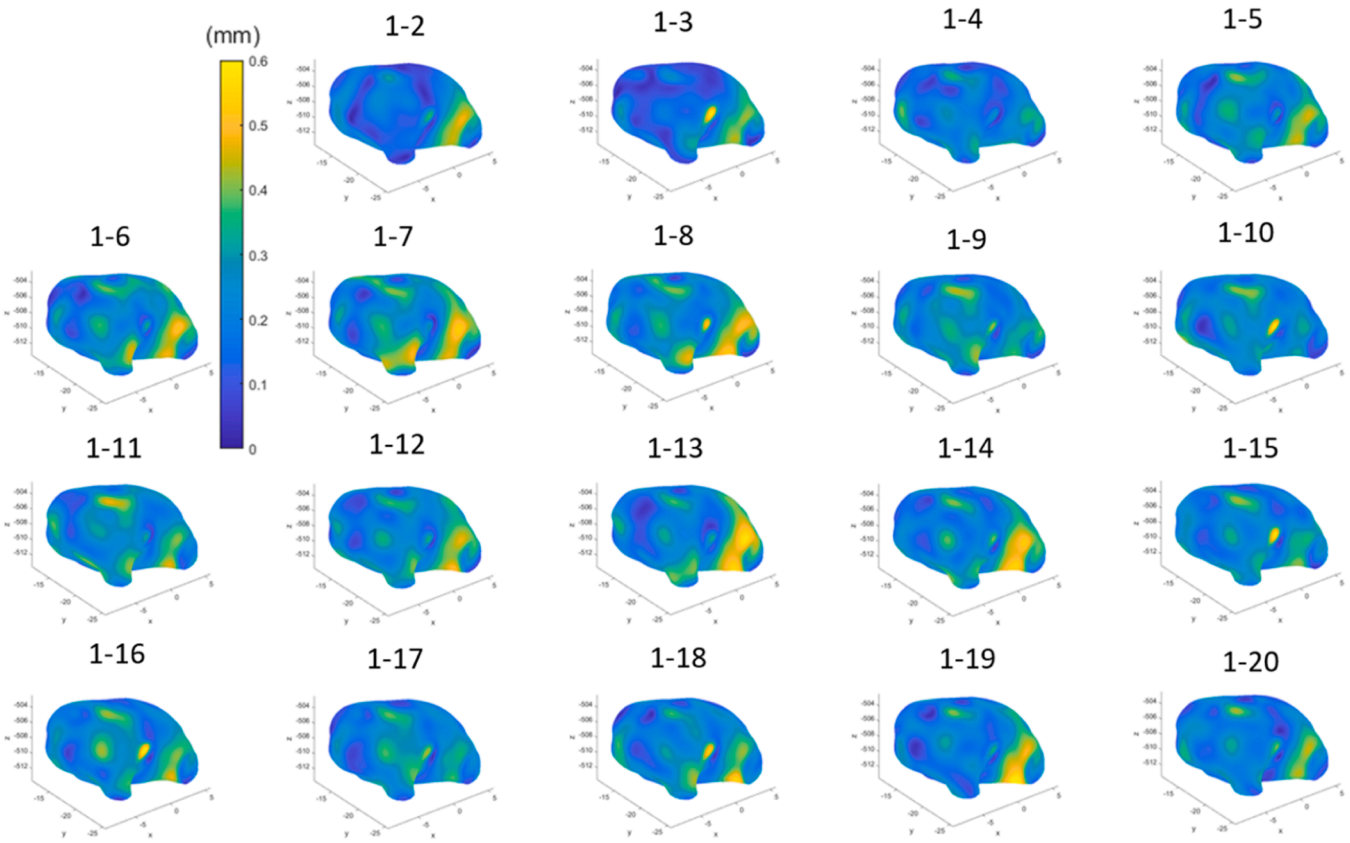


**Fig. 5.** The estimation results obtained by the CPD method.

attributable to human factors, and accurate estimation of aneurysm surface deformation can help clinicians identify irregular pulsations in aneurysms. Therefore, the primary objective of this study is to conduct deformation estimation of the aneurysm surface utilizing 4D-CTA image data [38].

In this paper, a novel method is proposed for the estimation of aneurysm surface deformation. The technique transforms the estimation problem into a constrained optimization problem, wherein the deformation of the aneurysm surface is estimated under the constrained optimization problem. This approach is based on a finite element deformation model, which employs an optimal constrained estimate of the mechanical deformation of the aneurysm surface, utilizing the sparsely collected local surface displacement data points. Simulation and experimental results demonstrate the efficacy of the proposed method in estimating aneurysm surface deformation.

## 2. Methods

### 2.1. Problem definition

Due to the complex structure and composition of the aneurysm, the wall deformation of the IAs exhibits a complex mechanical behaviour. However, the linear elasticity theory can accurately represent the mechanical deformation of soft tissues in a short period. Biological soft tissues exhibit linear elasticity at <15% of strain conditions [39]. Also, the deformation of the IA wall is very small compared to the size of the aneurysm, so the deformation of the IA wall can be assumed to be linearly elastic [40].

The strain energy function of the IA wall can be defined as

$$\boldsymbol{E}_{strain} = \frac{1}{2}\int_{\Omega} \boldsymbol{\varepsilon}^{\mathrm{T}}\boldsymbol{\sigma} d\Omega \tag{1}$$

Where $\boldsymbol{\varepsilon}$ represents the strain tensor, $\boldsymbol{\sigma}$ represents the stress tensor, and Ω represents the solution domain.

The stress tensor $\boldsymbol{\sigma}$ can be defined as

$$\boldsymbol{\sigma} = \boldsymbol{D}\boldsymbol{\varepsilon} \tag{2}$$

Where $\boldsymbol{D}$ is the material matrix, including Young's modulus $E$ and Poisson's ratio $\nu$.

The strain tensor $\boldsymbol{\varepsilon}$ can be defined as

$$\boldsymbol{\varepsilon} = \boldsymbol{B}\boldsymbol{U} \tag{3}$$

Where $\boldsymbol{B}$ represents the strain-displacement matrix, and $\boldsymbol{U}$ represents the nodal displacement in the solution domain of IA wall deformation.

For the static equilibrium system, the external force $\boldsymbol{F}$ equal to the internal force $\boldsymbol{R}$ as follows

$$\boldsymbol{R} - \boldsymbol{F} = 0 \tag{4}$$

Under finite element formulation, the internal force $\boldsymbol{R}$ can be obtained by

$$\boldsymbol{R} = \boldsymbol{K}\boldsymbol{U} \tag{5}$$

Where $\boldsymbol{K}$ is the stiffness matrix that embeds the discretized model equations, and the displacement $\boldsymbol{U}$ needs to be determined to construct the IAs wall deformation.

In this paper, we formulate the aneurysm surface deformation problem as a constrained estimation problem, i.e., the full nodal displacement $\boldsymbol{U}$ must reasonably match the sparse data points $\boldsymbol{y}$ which are measured from the aneurysm local surface. These sparse data points can be obtained by various imaging techniques, such as CTA and MRI [41]. Therefore, the IAs wall deformation model described by Eq. (5) is subject to the constraint as follows

$$\boldsymbol{y} = \boldsymbol{H}\boldsymbol{U} \tag{6}$$

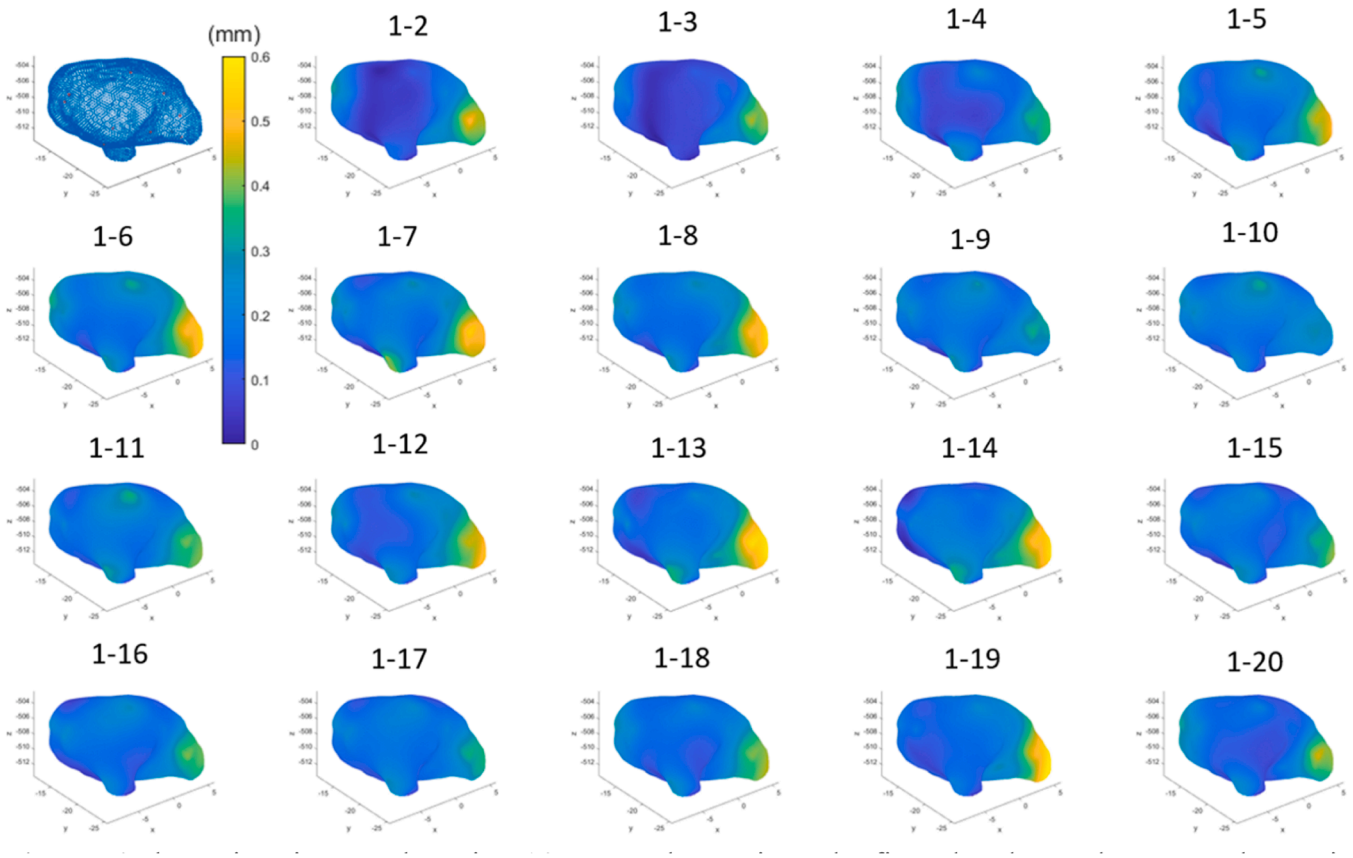


**Fig. 6.** The estimation results using 10 sparse data points: the first plot shows the sparse data points on the surface, and the remaining plots show the surface displacements with the first phase as a reference, for example, the estimated surface deformation from phase 1 to phase 2 are plotted as (1-2).

Where $H$ is the sampling matrix that maps the sparse data points $\boldsymbol{y}$ to the estimated solution $\boldsymbol{U}$.

From Eq. (4), we can have

$$\boldsymbol{U} = \boldsymbol{K}^{-1}\boldsymbol{R} \tag{7}$$

Then, denoting the estimated $\boldsymbol{U}$ by $\widetilde{\boldsymbol{U}}$ and estimated $\boldsymbol{R}$ by $\widetilde{\boldsymbol{R}}$, the Eq. (6) and (7) can be rewritten as

$$\widetilde{\boldsymbol{y}} = \boldsymbol{H}\widetilde{\boldsymbol{U}} \tag{8}$$

$$\widetilde{\boldsymbol{U}} = \boldsymbol{K}^{-1}\widetilde{\boldsymbol{R}} \tag{9}$$

Since $\widetilde{\boldsymbol{R}}$ is unknown, it is not possible to use Eq. (9) to calculate $\widetilde{\boldsymbol{U}}$, so it is reasonable first to estimate $\widetilde{\boldsymbol{R}}$, then use the estimated $\widetilde{\boldsymbol{R}}$ to obtain $\widetilde{\boldsymbol{U}}$.

### 2.2. Constrained estimation

The model data misfit ε can be obtained by Eq. (8) and (9) as follows

$$\epsilon = \boldsymbol{y} - \widetilde{\boldsymbol{y}} = \boldsymbol{y} - \boldsymbol{H}\boldsymbol{K}^{-1}\widetilde{\boldsymbol{R}} \tag{10}$$

The objective is to minimize the model data misfit ε between the model estimated. $\widetilde{\boldsymbol{U}}$ and measured sparse data points $\boldsymbol{y}$.

By optimal the minimization process of ε, the Eq. (10) can be written as

$$\boldsymbol{y} = \boldsymbol{H}\boldsymbol{K}^{-1}\widetilde{\boldsymbol{R}} \tag{11}$$

Thus, the minimization problem can be defined as $\text{argmin}E[(\boldsymbol{R}-\widetilde{\boldsymbol{R}})^{\mathrm{T}}(\boldsymbol{R}-\widetilde{\boldsymbol{R}})]$

$$\text{s.t. } \boldsymbol{y} = \boldsymbol{H}\boldsymbol{K}^{-1}\widetilde{\boldsymbol{R}} \tag{12}$$

Where $\boldsymbol{E}[\,\cdot\,]$ stands the expectation.

From Eq. (12), we can derive the objective cost function as follows

$$\boldsymbol{J} = E\left[(\boldsymbol{R}-\widetilde{\boldsymbol{R}})^{\mathrm{T}}(\boldsymbol{R}-\widetilde{\boldsymbol{R}})\right] + 2\lambda^{\mathrm{T}}\left(\boldsymbol{y}-\boldsymbol{H}\boldsymbol{K}^{-1}\widetilde{\boldsymbol{R}}\right) \tag{13}$$

Where $\lambda$ stands the Lagrange multiplier.

By expanding Eq. (13), we can have

$$\begin{aligned}\boldsymbol{J} &= \int (\boldsymbol{R}-\widetilde{\boldsymbol{R}})^{\mathrm{T}}(\boldsymbol{R}-\widetilde{\boldsymbol{R}})f(\boldsymbol{R})d\boldsymbol{R} + 2\lambda^{\mathrm{T}}\left(\boldsymbol{y}-\boldsymbol{H}\boldsymbol{K}^{-1}\widetilde{\boldsymbol{R}}\right)\\ &= \int \boldsymbol{R}^{\mathrm{T}}\boldsymbol{R}f(\boldsymbol{R})d\boldsymbol{R} - 2\int \widetilde{\boldsymbol{R}}^{\mathrm{T}}\boldsymbol{R}f(\boldsymbol{R})d\boldsymbol{R} + \widetilde{\boldsymbol{R}}^{\mathrm{T}}\widetilde{\boldsymbol{R}} + 2\lambda^{\mathrm{T}}\left(\boldsymbol{y}-\boldsymbol{H}\boldsymbol{K}^{-1}\widetilde{\boldsymbol{R}}\right)\\ &= \int \boldsymbol{R}^{\mathrm{T}}\boldsymbol{R}f(\boldsymbol{R})d\boldsymbol{R} - 2\widetilde{\boldsymbol{R}}^{\mathrm{T}}\int \boldsymbol{R}f(\boldsymbol{R})d\boldsymbol{R} + \widetilde{\boldsymbol{R}}^{\mathrm{T}}\widetilde{\boldsymbol{R}} + 2\lambda^{\mathrm{T}}\left(\boldsymbol{y}-\boldsymbol{H}\boldsymbol{K}^{-1}\widetilde{\boldsymbol{R}}\right)\end{aligned} \tag{14}$$

where $\boldsymbol{f}(\boldsymbol{R})$ is the conditional probability density function of $\boldsymbol{R}$.

The conditional mean of $\boldsymbol{R}$ can be expressed as

$$\overline{\boldsymbol{R}} = \int \boldsymbol{R}f(\boldsymbol{R})d\boldsymbol{R} \tag{15}$$

Substituting Eq. (15) into Eq. (14) yields

$$\boldsymbol{J} = \int \boldsymbol{R}^{\mathrm{T}}\boldsymbol{R}f(\boldsymbol{R})d\boldsymbol{R} - 2\widetilde{\boldsymbol{R}}^{\mathrm{T}}\overline{\boldsymbol{R}} + \widetilde{\boldsymbol{R}}^{\mathrm{T}}\widetilde{\boldsymbol{R}} + 2\lambda^{\mathrm{T}}\left(\boldsymbol{y}-\boldsymbol{H}\boldsymbol{K}^{-1}\widetilde{\boldsymbol{R}}\right) \tag{16}$$

By taking the partial derivatives of Eq. (16) with respect to $\widetilde{\boldsymbol{R}}$ and $\lambda$ and letting them equal to zero, we can have

$$\frac{d\boldsymbol{J}}{d\widetilde{\boldsymbol{R}}} = -2\overline{\boldsymbol{R}} + 2\widetilde{\boldsymbol{R}} - 2\left(\boldsymbol{H}\boldsymbol{K}^{-1}\right)^{\mathrm{T}}\lambda = 0 \tag{17}$$

$$\frac{d\boldsymbol{J}}{d\lambda} = 2\left(\boldsymbol{y}-\boldsymbol{H}\boldsymbol{K}^{-1}\widetilde{\boldsymbol{R}}\right) = 0 \tag{18}$$

Rearrange Eq. (17), we can have

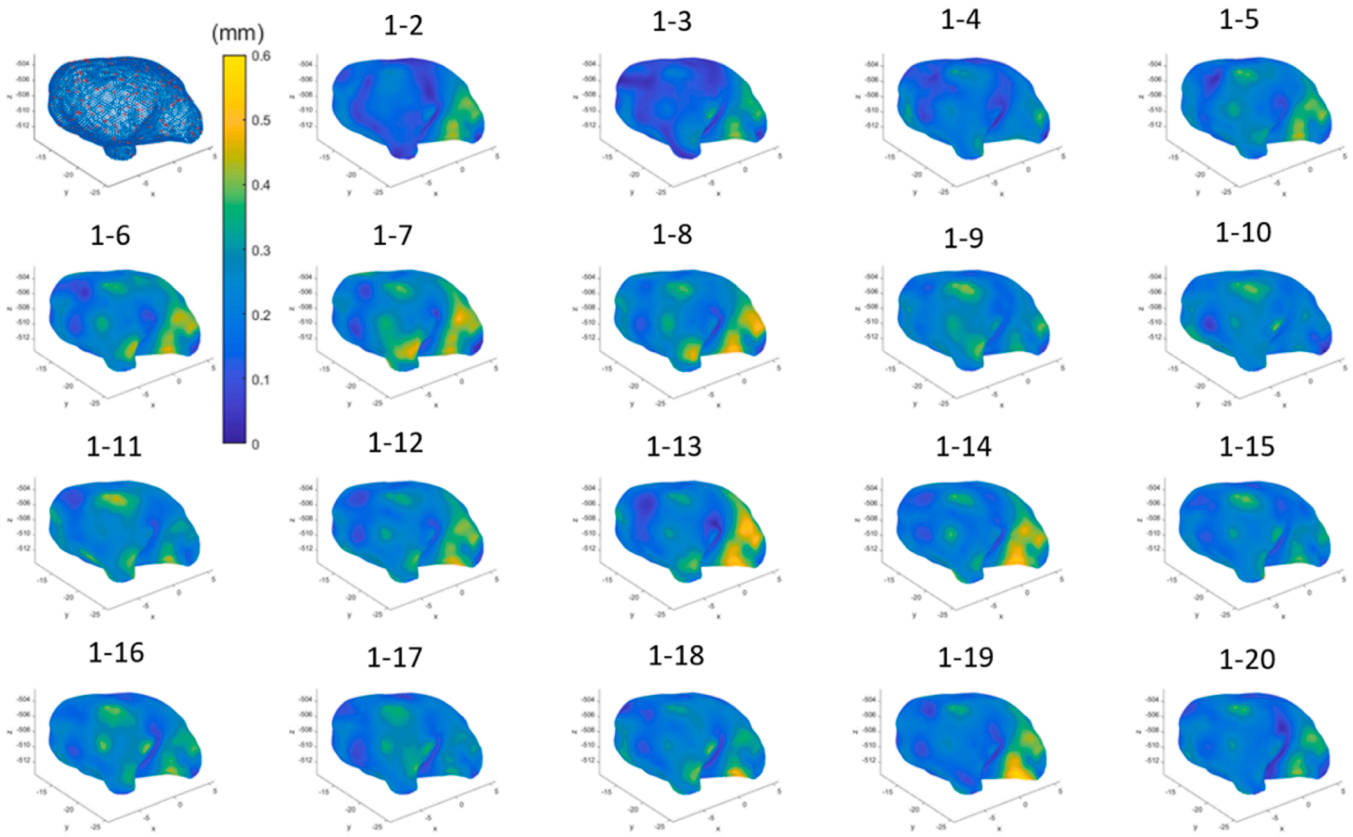


**Fig. 7.** The estimation results using 300 sparse data points.

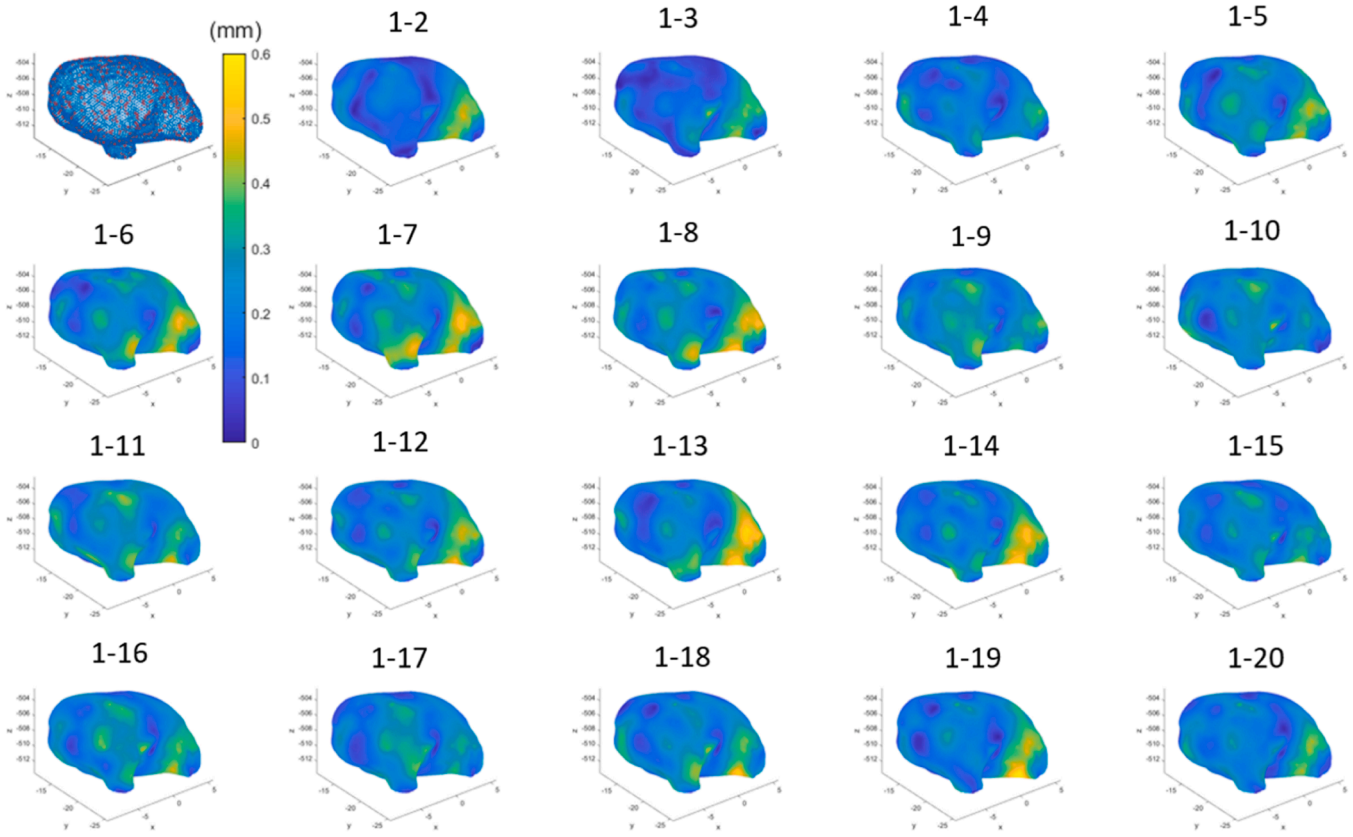


**Fig. 8.** The estimation results using 600 sparse data points.

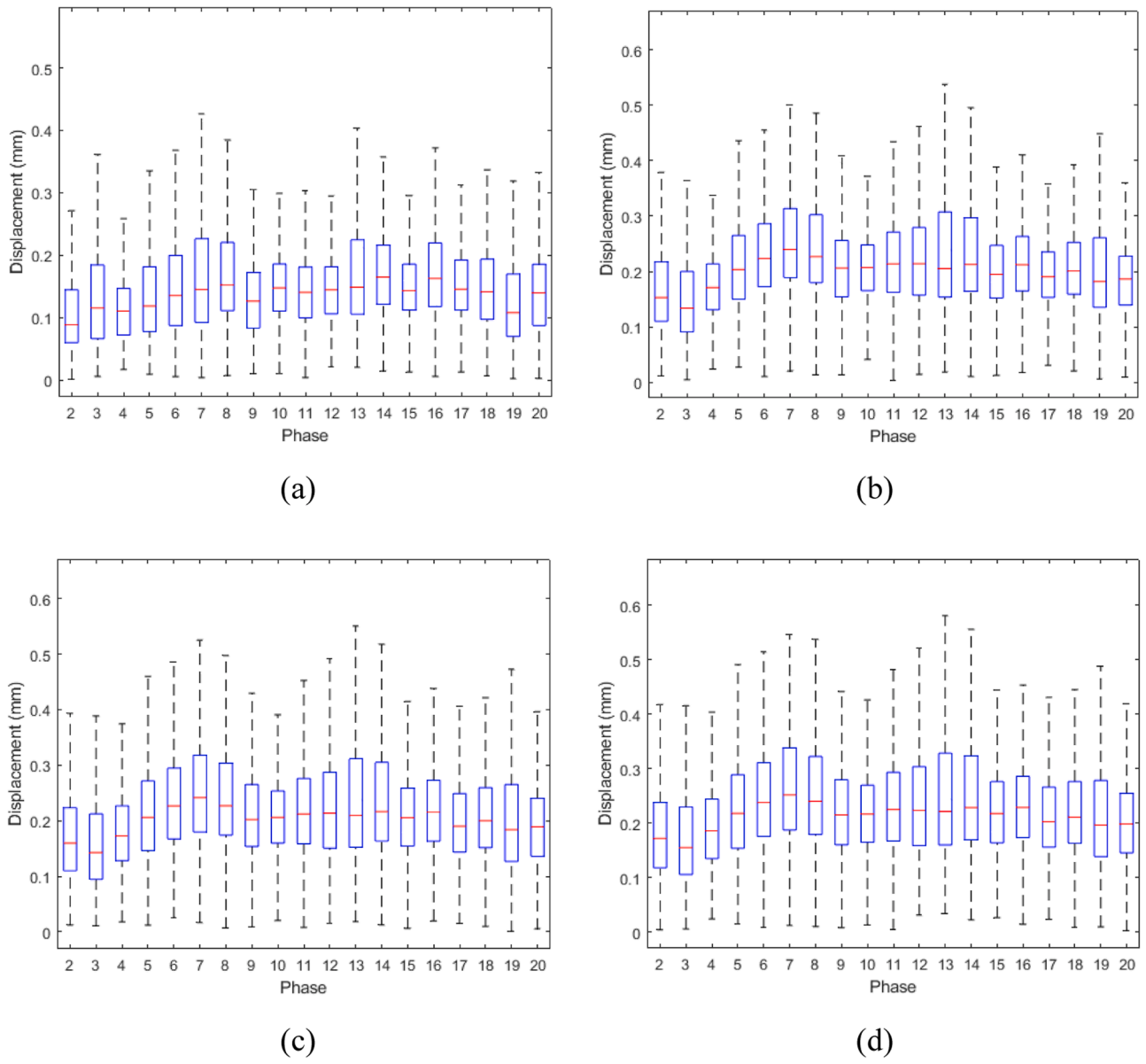


**Fig. 9.** Boxplot of the displacement at each phase by using the different number of sparse data points: (a) 10 sparse data points; (b) 300 sparse data points; (c) 600 sparse data points; (d) The CPD estimation.

**Table 2**
Statistical error analysis of constrained estimation by using different numbers of sparse data points.

| $N_{sprs}$ | Mean Square Error | Mean Absolute Error | Root Mean Square Deviation |
|---|---|---|---|
| 10 | 0.01502 | 0.09256 | 0.12211 |
| 50 | 0.00698 | 0.06073 | 0.08337 |
| 100 | 0.00526 | 0.04993 | 0.07232 |
| 200 | 0.00306 | 0.03628 | 0.05518 |
| 300 | 0.00283 | 0.03203 | 0.05300 |
| 400 | 0.00242 | 0.02832 | 0.04900 |
| 500 | 0.00218 | 0.02501 | 0.04648 |
| 600 | 0.00210 | 0.02302 | 0.04559 |

$$\widetilde{\boldsymbol{R}} = \overline{\boldsymbol{R}} + \left(\boldsymbol{H}\boldsymbol{K}^{-1}\right)^{\mathrm{T}}\boldsymbol{\lambda} \tag{19}$$

Multiplying both sides of Eq. (19) by $\boldsymbol{H}\boldsymbol{K}^{-1}$ to obtain

$$\boldsymbol{H}\boldsymbol{K}^{-1}\,\widetilde{\boldsymbol{R}} = \boldsymbol{H}\boldsymbol{K}^{-1}\,\overline{\boldsymbol{R}} + \boldsymbol{H}\boldsymbol{K}^{-1}\,\left(\boldsymbol{H}\boldsymbol{K}^{-1}\right)^{\mathrm{T}}\boldsymbol{\lambda} \tag{20}$$

Substituting Eq. (20) into Eq. (18) yields

$$2\left(\boldsymbol{y} - \boldsymbol{H}\boldsymbol{K}^{-1}\overline{\boldsymbol{R}} - \boldsymbol{H}\boldsymbol{K}^{-1}\left(\boldsymbol{H}\boldsymbol{K}^{-1}\right)^{\mathrm{T}}\boldsymbol{\lambda}\right) = 0 \tag{21}$$

From Eq. (21), we can obtain $\boldsymbol{\lambda}$ as follows

$$\boldsymbol{\lambda} = \left(\boldsymbol{H}\boldsymbol{K}^{-1}\left(\boldsymbol{H}\boldsymbol{K}^{-1}\right)^{\mathrm{T}}\right)^{-1}\left(\boldsymbol{y} - \boldsymbol{H}\boldsymbol{K}^{-1}\overline{\boldsymbol{R}}\right) \tag{22}$$

By substituting $\boldsymbol{\lambda}$ into Eq. (19) to obtain

$$\widetilde{\boldsymbol{R}} = \overline{\boldsymbol{R}} + \left(\boldsymbol{H}\boldsymbol{K}^{-1}\right)^{\mathrm{T}}\left(\boldsymbol{H}\boldsymbol{K}^{-1}\left(\boldsymbol{H}\boldsymbol{K}^{-1}\right)^{\mathrm{T}}\right)^{-1}\left(\boldsymbol{y} - \boldsymbol{H}\boldsymbol{K}^{-1}\overline{\boldsymbol{R}}\right) \tag{23}$$

Rewrite Eq. (23) into recursive form

$$\widetilde{\boldsymbol{R}}_{k+1} = \widetilde{\boldsymbol{R}}_{k} + \left(\boldsymbol{H}\boldsymbol{K}^{-1}\right)^{\mathrm{T}}\left(\boldsymbol{H}\boldsymbol{K}^{-1}\left(\boldsymbol{H}\boldsymbol{K}^{-1}\right)^{\mathrm{T}}\right)^{-1}\left(\boldsymbol{y}_{k} - \boldsymbol{H}\boldsymbol{K}^{-1}\widetilde{\boldsymbol{R}}_{k}\right) \tag{24}$$

Where $\widetilde{\boldsymbol{R}}_{0} = \overline{\boldsymbol{R}}$ and $k$ is the iteration number.

According to Eq. (9), multiplying both sides of Eq. (24) by $\boldsymbol{K}^{-1}$, we can have

$$\widetilde{\boldsymbol{U}}_{k+1} = \widetilde{\boldsymbol{U}}_{k} + \boldsymbol{L}\left(\boldsymbol{y}_{k} - \boldsymbol{H}\widetilde{\boldsymbol{U}}_{k}\right) \tag{25}$$

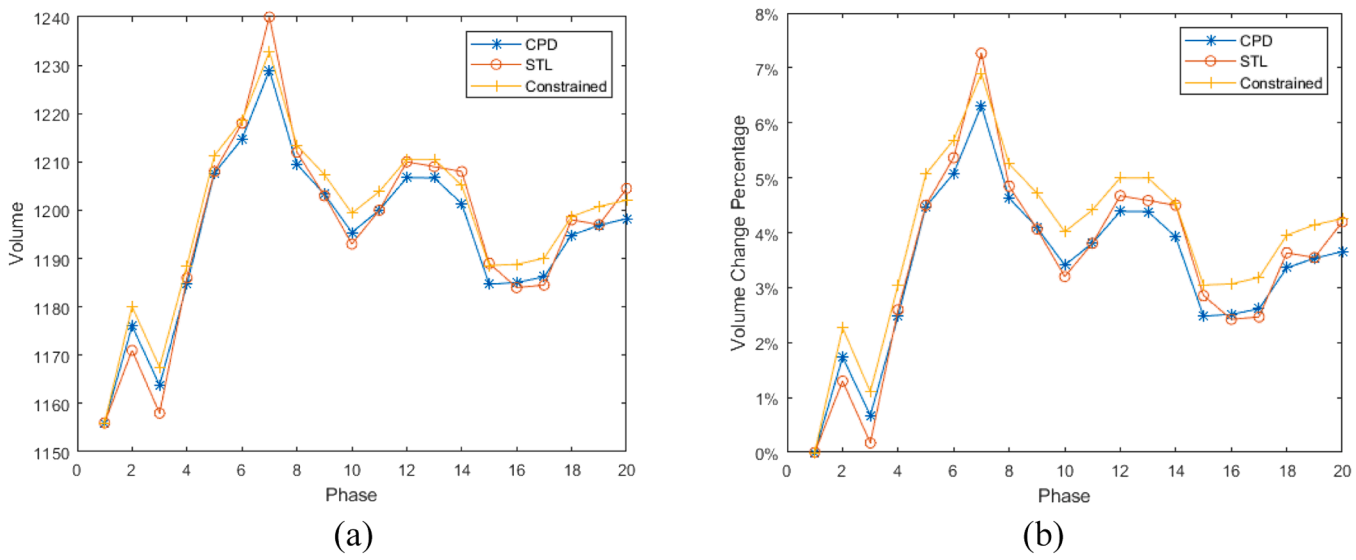


**Fig. 10.** Volume ($mm^3$)change in different phases: (a) volume change; (b) volume change percentage.

Where

$$\boldsymbol{L} = \boldsymbol{K}^{-1}\left(\boldsymbol{H}\boldsymbol{K}^{-1}\right)^{\mathrm{T}}\left(\boldsymbol{H}\boldsymbol{K}^{-1}\left(\boldsymbol{H}\boldsymbol{K}^{-1}\right)^{\mathrm{T}}\right)^{-1} \tag{26}$$

Therefore, the estimation of aneurysm surface deformation can be summarised into the following steps:

(i) Set $\widetilde{\boldsymbol{U}}_0$ for the initial condition,
(ii) Calculate the matrix $\boldsymbol{L}$,
(iii) For each iteration,

- Conduct constrained estimation using (25).

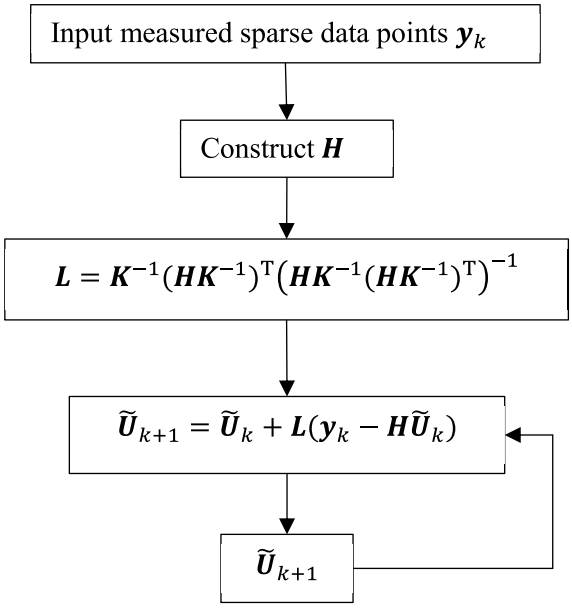


## 3. Results

Simulations and practical experimental analyses are carried out to validate the proposed constrained estimation method. Firstly, we simulate a simple cubic model intending to demonstrate the feasibility of the proposed method. We discussed the effect of the number of sparse data points on the constrained estimation results and compared it with finite element analysis (FEA) reference results. We then performed a constrained estimation of the intracranial aneurysm model based on patient-specific 4D-CTA imaging. Then we compared it with the well-known point set registration technique, coherent point drift (CPD) [42]. Finally, we performed an experimental analysis to validate the proposed method further. In the experimental study, we performed compression tests on a cubic model made of silica gel, and the sparse data point displacements on the cube's surface were obtained by an optical coherence tomography (OCT) imaging system and used for constrained estimation. A FEA was then performed and validated against the constrained estimation results.

### 3.1. Cubic model

Consider the deformation on a simple cubic model, as shown in Fig. 1 (a). This cubic model is $10cm \times 10cm \times 10cm$, uniformly meshed with 386 surface nodes, and material properties of the cubic sample are 0.2 for the Poisson's ratio and $3000Pa$ for the Young's modulus. The cubic model is fixed at the bottom and compressed on its left side to generate the deformation using FEA. The FEA deformation result will be used as a data set and reference value for constrained estimation. Fig. 1(b) shows the FEA deformation result, which will be used as a reference value and Fig. 1(c) shows the surface point cloud. The deformed point cloud is shown in Fig. 1(d), and the compression between the original point cloud (blue) and the deformed point cloud (red) has been demonstrated in Fig. 1 (e) and the front view in Fig. 1(f).

The simulation process was carried out by matching blue points to red points using constrained estimation and then comparing them to the FEA reference values. Fig. 2 shows the results of the constrained estimation by using different numbers of sparse data points. Fig. 2(a) shows the sparse data points on the surface (red), Fig. 2(b) and (c) shows the estimated results (blue) compared to the FEA results (red), and Fig. 2(d) shows a colour map of the estimated results. As the number of sparse data points increases, the displacement field approaches the reference results obtained from FEA simulations. In Fig. 2, the estimation result using only one sparse point inadequately captured the deformation distribution of the cubic surface compared to the FEA reference solution shown in Fig. 1(e) and (f). In Fig. 2, when we use four vertices as sparse data points, we find that the accuracy of the constrained estimation is greatly improved because these four vertices can represent the topological features of the cubic model, which indicates that the proposed method can significantly improve the accuracy of the estimation when the structural features of the model can be traced. In Fig. 2, when we

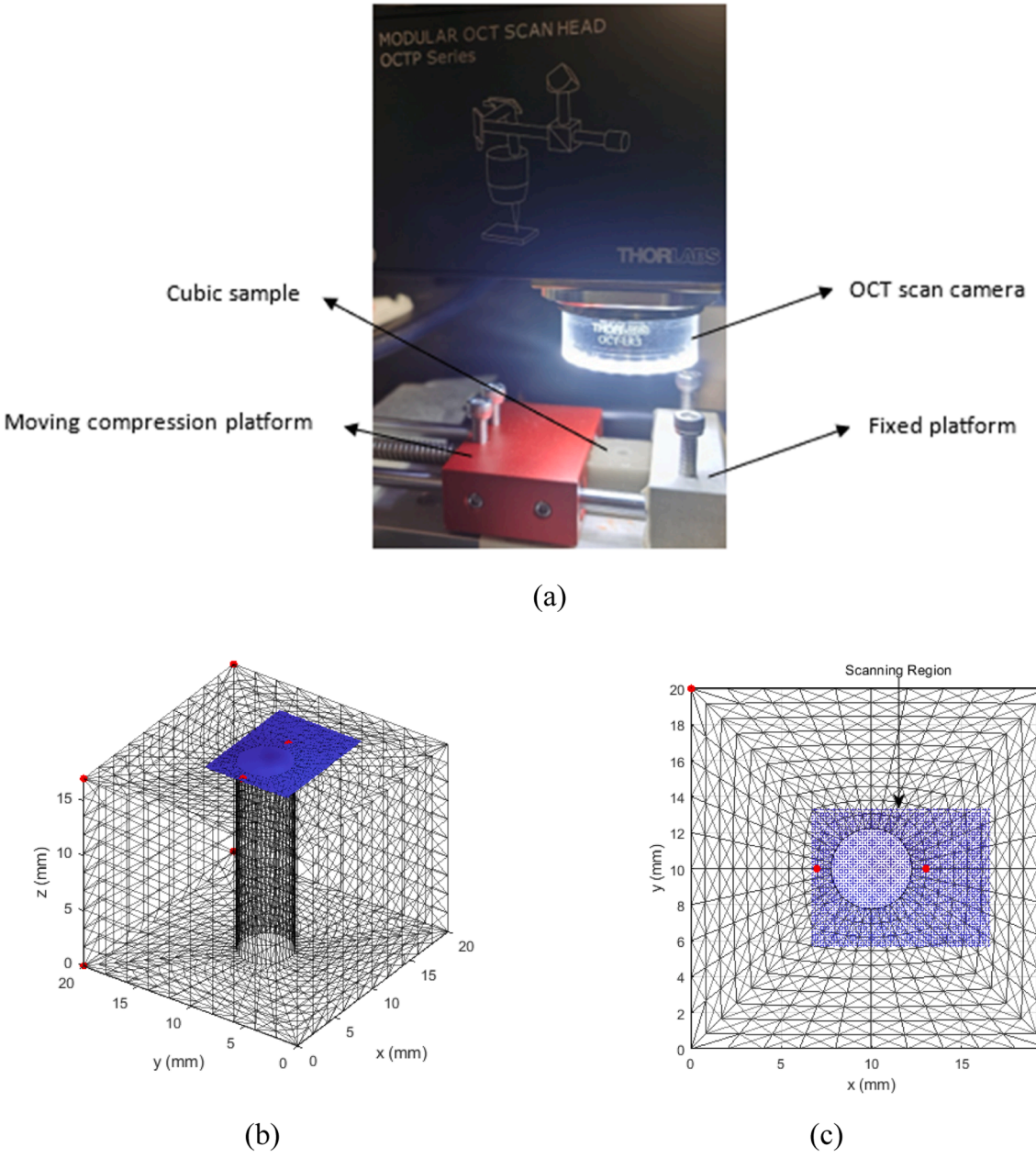


**Fig. 11.** (a) The experiment setup; (b) The cubic model utilized in the simulation was subjected to the same boundary conditions as the experimental setup. The bottom surface ($y = 0mm$) was assumed to be fixed, while the top surface ($y = 20mm$) was compressed and scanning region in blue; (c) The front view of the cubic model.

increase the number of sparse data points to 50, the constrained estimates are already very close to the results of the FEA in Fig. 1(e) and (f). When 100 sparse data points are used, the constrained estimation results are almost identical to those of the FEA. We can see no significant visual difference between the colourmap plot estimated using 50 and 100 sparse data points and the FEA reference result in Fig. 1(b). This trend can also be seen in the statistical errors in Table 1, where we can see that the errors decrease as the number of sparse data points increases, with sufficient accuracy being reached when 50 sparse data points are used.

### 3.2. Intracranial aneurysm model

#### 3.2.1. Simulation procedures

The intracranial aneurysm model used in this study was constructed from patient-specific imaging data obtained from the Renji Hospital, Shanghai, China, from existing databases and was approached and conducted in accordance with the guidelines and regulations established by the Queensland University of Technology Human Research Ethics Committee (Project Reference ID: 2022-6108-10078), and written informed consent was obtained from all participants before their inclusion in the study. The proposed method requires data processing. Since the method is based on 4D-CTA image data for displacement estimation, segmentation of the 4D-CTA image data is needed before constrained estimation to obtain all three-dimensional models of the aneurysm during the cardiac cycle.

A 320-detector row CT scanner (Aquilion ONE VISION, Canon Medical System Corporation, Otawara, Japan) was used to scan the cerebral arteries with a prospective ECG-gated scan mode performed during one cardiac cycle. The spatial resolution of the 4D-CTA data is $0.31 \times 0.31 \times 0.5\ mm^3$. The 4D-CTA scans were performed during one cardiac cycle using a prospective ECG-gated scanning mode, and the reconstruction included 20 phases of R-R interval from 0% to 95% every

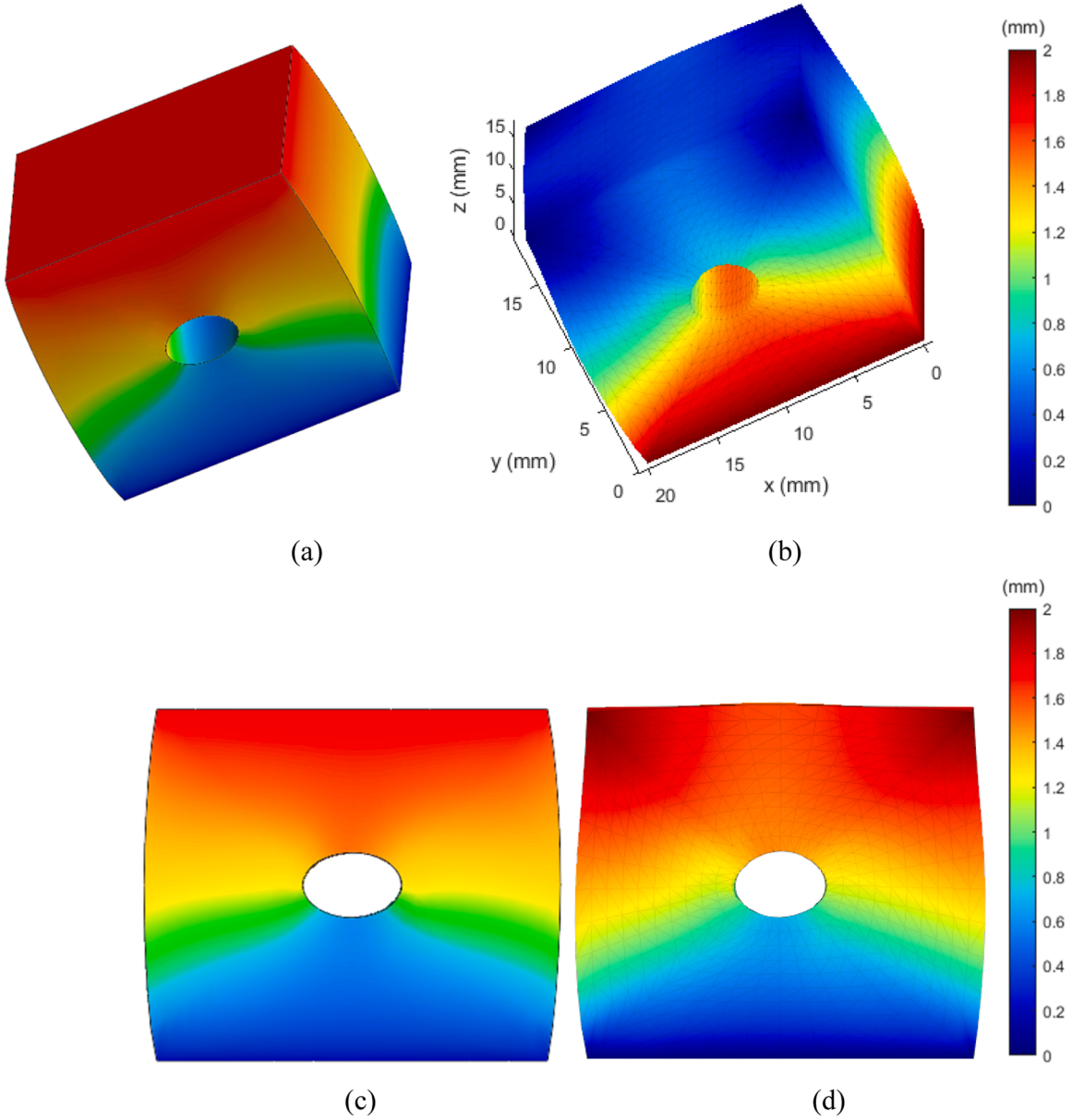


**Fig. 12.** The simulation results were obtained by (a) Reference solution; (b) Constrained estimation. The front view of the cubic model modelling results obtained by (a) Reference solution; (b) Constrained estimation.

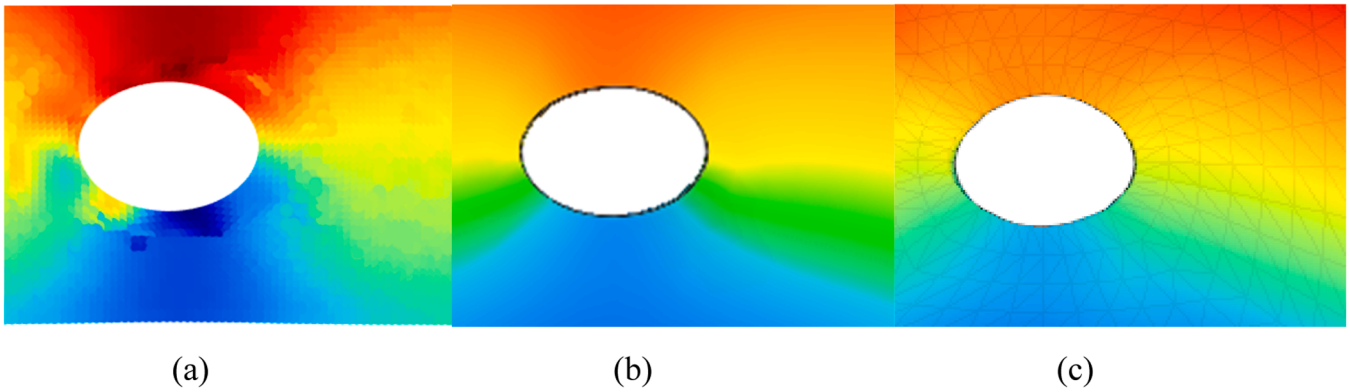


**Fig. 13.** The deformation field for the scanning region: (a) DVC result; (b) Reference solution; (c) Constrained estimation.

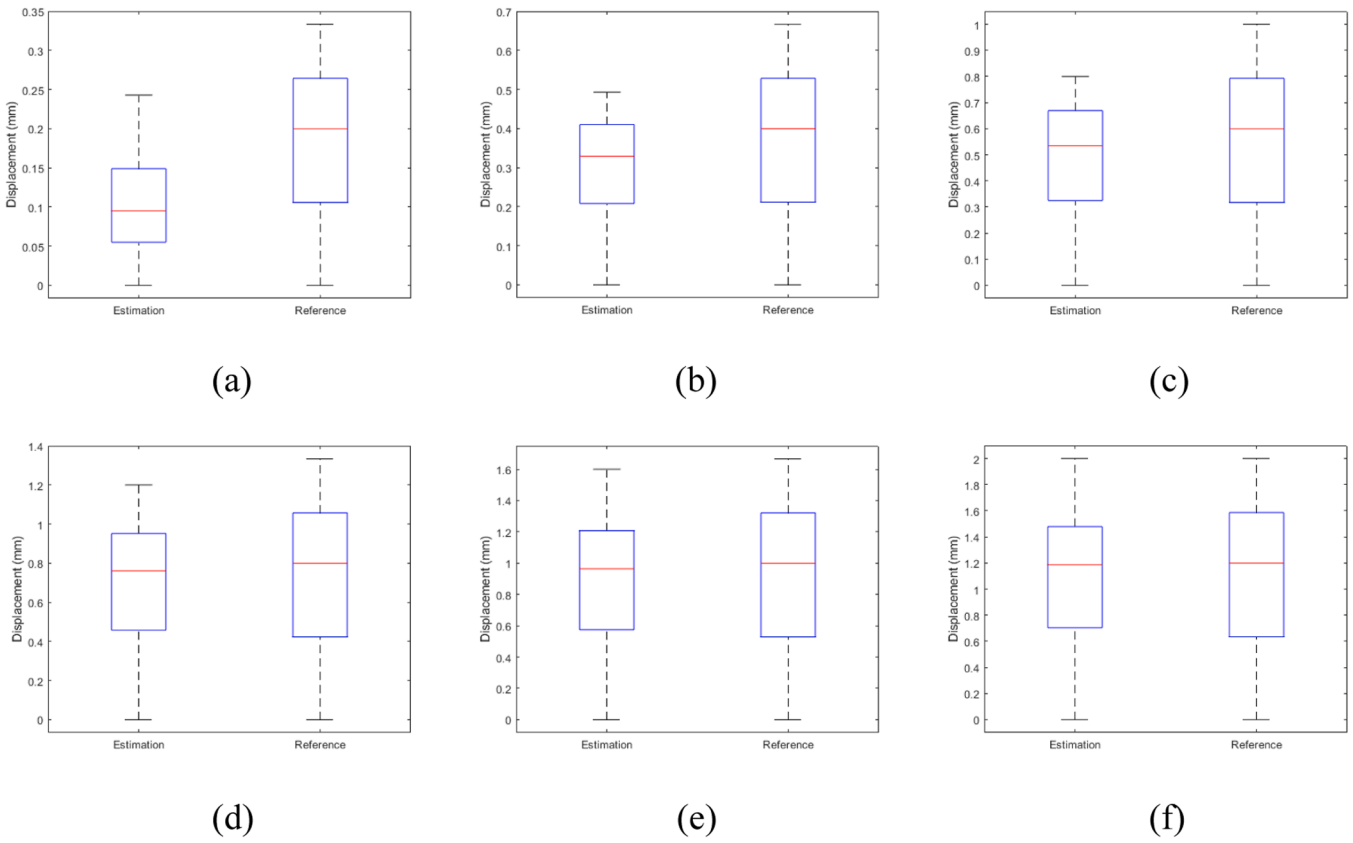


**Fig. 14.** Displacement plots obtained by the reference solution and constrained estimation at different compression steps: (a) step 1; (b) step 2; (c) step 3; (d) step 4; (e) step 5; (f) step 6.

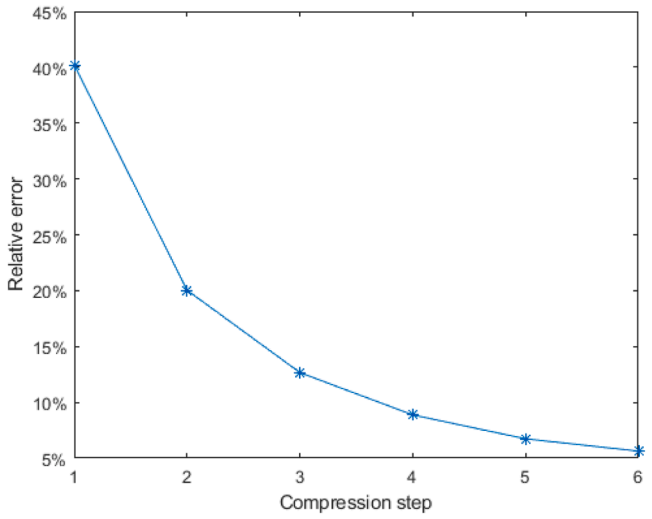


**Fig. 15.** The relative error with compression steps.

5% cardiac cycle, and the detailed protocol can be found in previous publication [37]. Fig.. 3 shows the segmentation procedure for constructing patient-specific intracranial aneurysm 3D models using 4D-CTA imaging data, and the size of this patient's aneurysm is 14 *mm*. These 20 phases are generated from one cardiac cycle with an elapsed time of around 1 second. After obtaining the 3D model of the aneurysm based on the 4D-CTA imaging data, the aneurysm was reduced to only the region of interest. The phase 1 model was meshed into 5815 surface nodes, as shown in Fig. 4. The patient-specific intracranial aneurysm model was first simulated by CPD based on phase 1 to generate the displacement field of the aneurysm surface for the rest of the 19 phases. These nodes and their displacements were used as a pooled sample ($N_{total}$= 5815), the spares data points were randomly selected points on the aneurysm surface, which were then used for constrained estimation.

### 3.2.2. *Simulation results*

Fig. 5 displays the deformation results obtained from the CPD simulations at different phases, which serve as reference results. Figs. 6–8 depict the estimated results obtained using different numbers of sparse data points. As the number of sparse data points increases, the displacement field approaches the CPD estimation results. In Fig. 6, the constrained estimation employs 10 sparse data points, inadequately capturing the aneurysm surface deformation compared to the CPD estimation results shown in Fig. 5. Similarly, the overall displacement at each phase shown in Fig. 9(a) does not match well compared to the CPD estimation displayed in Fig. 9(d). Therefore, in later simulations, the sparse data points gradually increased. The study further increases the sparse data points to 300 for higher accuracy, as presented in Fig. 7. It displays more surface deformation features visible in the contour distribution compared to Fig. 5. Fig. 9(b) shows that the displacement distribution at each phase is closer to the CPD estimation in Fig. 9(d). We further increase the number of sparse data points to 600, and the estimation results are shown in Fig. 8, which are closer to the CPD estimation in Fig. 5. In Fig. 9(c), the displacement distribution at each phase is almost identical to the CPD estimation in Fig. 9(d). Table 2 shows that the error decreases as the number of sparse data points increases. The mean square error, mean absolute error, and root mean square deviation converge at around 0.002, 0.02 and 0.04, respectively, which suggests that using approximately 600 sparse data points is sufficient to achieve adequate accuracy. Finally, we compare the volume changes in Fig. 10, where STL represents the volume of the original 3D model (STL file)

obtained by segmentation. The volume change of the aneurysm obtained from the CPD and constrained estimations using 600 sparse data points are then compared with the original STL file. We can see that the volume change of both estimation methods is very close to the volume change of the original 3D model. This indicates that the proposed constrained estimation method is accurate when using sufficiently sparse data points.

### 3.3. Experimental analysis

#### 3.3.1. Experimental procedures

The experimental analysis was performed on a cubic model made of silica gel with dimensions of $20mm \times 20mm \times 17mm$ and with a hollow cube at a $4.5mm$ diameter. The material properties of the cubic sample are a Poisson's ratio of 0.47, a density of $1000kg/m^3$ and Young's modulus of $1.4MPa$. Fig. 11(a) shows the experiment setup, where the cubic sample is placed on a rigid platform and compressed from the top by a moving compression platform. An optical coherence tomography (OCT) imaging system with a digital volume correlation (DVC) algorithm [43] is used to capture and estimate the displacement within the imaged area. To mimic the experimental conditions, the cubic model used for FEA simulations and constrained estimation was modelled with the same boundary conditions. The cubic model is shown in Fig. 11(b), the nodes on the bottom ($y = 0mm$) of the cube model were assumed to be fixed. A prescribed displacement of $2mm$ was applied to the top surface ($y = 20mm$) of the cube model.

Firstly, FEA simulations were carried out, and the results were used as a reference solution and further compared with the constrained estimates for verification. The FEA simulations meshed the cubic model into 4840 nodes and 24000 tetrahedral elements, was the same as the cubic sample in terms of geometry, material properties and loading conditions. Fig. 11(b) and (c) show the scanning region of the OCT imaging system, represented as the blue region. The initial OCT images of the cubic sample were taken before any compression was applied. This served as a baseline for comparison with the compressed images, and then the prescribed displacement was applied to the cubic sample using for 6 compression stages ranging from $0mm$ to $2mm$. OCT images were taken at different compression levels to monitor the deformation of the cubic sample. The deformation of the cubic model was measured as it was compressed by analyzing OCT images using the DVC algorithm. Fig. 11(b) and (c) illustrate the selection of six sparse data points for the constrained estimation. Among these data points, two were located within the scanning area, while the remaining four were positioned at the top surface's corners. As the top surface was subjected to a prescribed displacement, the displacements of all nodes on this surface were known. However, only four vertices were selected as sparse data points for computational efficiency. This approach expedited the calculation process without compromising the accuracy of the estimation.

#### 3.3.2. Experimental results

Fig. 12 (a) and (b) show the deformation results obtained from the FEA reference solution and the constrained estimation. We can see that the overall displacement field obtained from the constrained estimation is very close to the reference solution. To further study the simulation results, the front view of the modelling results of the cubic model obtained by both methods was plotted in Fig. 12 (c) and (d), and we can see a slight difference in the surrounding region of the hole because we used only two sparse data points in this region, but the overall result is still acceptable. Fig. 13(a) shows the distribution of surface displacements estimated by DVC in the final compression step. However, the results are not entirely smooth due to noise in the measured data, and not all sparse data points can be used in the analysis. Fig. 13(b) and (c) show the FEA reference solutions and constrained estimation results for the scanned region, which are very similar to the displacement distribution of the DVC. In other words, we used the measured data from the OCT imaging system to reconstruct the overall deformation field of the cubic model. In Fig. 14, the displacements at different compression steps were plotted, and we can see that as the step increases, the results of the constrained estimation are closer to the FEA reference solution. This trend is also reflected in the relative error plot in Fig. 15, and the statistical errors of the constrained estimation are 0.02439 for the mean square error, 0.11598 for the mean absolute error, and 0.14364 for the root-mean-square deviation. The above analyses show that the proposed method can estimate the overall deformations of the cubic model from the measured data with relative accuracy.

## 4. Discussion

### 4.1. Contribution

Although haemodynamic parameters such as OSI, PLc and WSS are associated with the development and rupture of intracranial aneurysms, deformation of the surface of intracranial aneurysms [8,18], such as irregular pulsations, is also an important reference factor [37,44]. The proposed constrained estimation allows a reliable reconstruction of the surface deformation of intracranial aneurysms during a cardiac cycle based on sufficient sparse data points. The results estimated by the method presented in Section 3.2 are very similar to those estimated by the CPD method [42]. Compared with the CPD method, the proposed method is only based on sparse data points, and the $\boldsymbol{L}$ matrix in Eq. (25) can be precomputed after these sparse data points are identified, which improves the computational efficiency. Meanwhile, the global optimization of CPD requires high computational cost, especially when dealing with large point clouds. This may lead to longer processing time, especially on resource-limited devices.

Moreover, compared to purely imaging-based displacement estimation methods, such as the DVC algorithm [43] in Section 3.3, the proposed method exploits the laws of elastic physics and offers better accuracy. As demonstrated in Fig. 13(a), DVC estimation results are not as smooth as the proposed method, and the accuracy of DVC estimation is highly dependent on image quality. In medical imaging, where image quality can be compromised due to various factors, such as motion artifacts and image noise, this limitation can impact the accuracy of the displacement estimation. In contrast, the proposed method allows accurate displacement estimation using measurements from sparse data points by incorporation of physical laws.

### 4.2. Limitation

Despite its potential advantages, the proposed method has some limitations. Currently, the method focuses solely on homogeneous simulations and does not account for the inhomogeneous mechanical properties of the aneurysm, which is an essential consideration for future research. Therefore, further investigations are needed to address these limitations and explore the feasibility of incorporating inhomogeneous mechanical properties in the proposed method. Furthermore, the current method performs the simulation based on only one patient; with the analysis of data from multiple patients, our proposed method has the potential to detect any potential relationship between aneurysm surface deformation and the risk of aneurysm rupture. Alternatively, by analyzing more patient data, we aim to establish a correlation between hemodynamic parameters and aneurysm surface deformation, such as OSI, PLc and WSS. Moreover, it is noteworthy that the proposed method does not consider the possible presence of noise in the measurement data. However, in practical situations, measurement data is often subject to noise. We suggest incorporating a noise-filtering technique into the proposed method to address this issue. For instance, the Kalman filter [45] could be employed to enhance the method's robustness against measurement noise.

## 5. Conclusion

The accurate estimation of the deformation of the intracranial aneurysm surface is a critical parameter for assessing the risk of aneurysm rupture. This research aims to reconstruct patient-specific intracranial aneurysm surface deformation using a constrained estimation approach based on sparse data points. The proposed framework formulates the problem of aneurysm surface deformation as a constrained estimation problem, where the objective is to minimize the misfit error between the estimated and measured sparse data points. The performance of this approach is demonstrated through both simulation and experimental results, which show that accurate aneurysm surface deformation can be achieved by incorporating a sufficient number of sparse data points. Overall, this research provides a novel solution for estimating intracranial aneurysm surface deformation, which has important implications for the clinical management of aneurysms and the prevention of ruptures.

In future work, we hope to explore the potential relationship that may exist between aneurysm surface deformation and rupture risk by analyzing more patient data. In addition, after obtaining aneurysm surface displacements, we can calculate the strain of the aneurysm surface during the cardiac cycle. The distribution of aneurysm surface strain in low-risk aneurysms may differ from that in high-risk aneurysms. Based on a large amount of patient data, we aim to explore the potential correlation between the risk of aneurysm rupture and the distribution of aneurysm surface strain. Furthermore, measurement uncertainty is also an important topic in medical imaging and clinical research, especially when high accuracy and reproducibility are required. Therefore, quantitative assessment of measurement uncertainty based on 4D-CTA image datasets of multiple patients is needed to improve the credibility and applicability of studies.

## Statement of ethics

This study was approved by the Queensland University of Technology Human Research Ethics Committee (Project Reference ID: 2022-6108-10078), and written informed consent was obtained from all participants before their inclusion in the study.

## Declaration of Competing Interest

The authors declare that they have no known competing financial interests or personal relationships that could have appeared to influence the work reported in this paper.

## Acknowledgments

This work was partially supported by the Australian Research Council (ARC) (Grant Number DP200103492), the National Natural Science Foundation of China (Grant Numbers 12172089, 11972118, 61821002) and the Medical Research Future Fund (2016165).

## Supplementary materials

Supplementary material associated with this article can be found, in the online version, at doi:10.1016/j.cmpb.2023.107975.

## References

[1] R.D. Brown Jr, J.P. Broderick, Unruptured intracranial aneurysms: epidemiology, natural history, management options, and familial screening, Lancet Neurol. 13 (4) (2014) 393–404.
[2] W. Brinjikji, et al., Risk factors for growth of intracranial aneurysms: a systematic review and meta-analysis, Am. J. Neuroradiol. 37 (4) (2016) 615–620.
[3] J.P. Greving, et al., Development of the PHASES score for prediction of risk of rupture of intracranial aneurysms: a pooled analysis of six prospective cohort studies, Lancet Neurol. 13 (1) (2014) 59–66.
[4] N. Chalouhi, B.L. Hoh, D. Hasan, Review of cerebral aneurysm formation, growth, and rupture, Stroke 44 (12) (2013) 3613–3622.
[5] B.G. Thompson, et al., Guidelines for the management of patients with unruptured intracranial aneurysms: a guideline for healthcare professionals from the American heart association/American stroke ASSOCIATION, Stroke 46 (8) (2015) 2368–2400.
[6] M. Korja, R. Kivisaari, B.R. Jahromi, H. Lehto, Size and location of ruptured intracranial aneurysms: consecutive series of 1993 hospital-admitted patients, J. Neurosurg. 127 (4) (2016) 748–753.
[7] F. Mezali, S. Benmamar, K. Naima, H. Ameur, O. Rafik, Evaluation of stent effect and thrombosis generation with different blood rheology on an intracranial aneurysm by the lattice Boltzmann method, Comput. Methods Programs Biomed. 219 (2022), 106757.
[8] B. Kurşun, L. Uğur, G. Keskin, Hemodynamic effect of bypass geometry on intracranial aneurysm: A numerical investigation, Comput. Methods Programs Biomed. 158 (2018) 31–40.
[9] F. Mezali, K. Naima, S. Benmamar, A. Liazid, Study and modeling of the thrombosis of small cerebral aneurysms, with and without flow diverter, by the lattice Boltzmann method, Comput. Methods Programs Biomed. 233 (2023), 107456.
[10] M. Zimny, E. Kawlewska, A. Hebda, W. Wolański, P. Ładziński, W. Kaspera, Wall shear stress gradient is independently associated with middle cerebral artery aneurysm development: a case-control CFD patient-specific study based on 77 patients, BMC Neurol. 21 (1) (2021) 1–10.
[11] Y. Murayama, S. Fujimura, T. Suzuki, H. Takao, Computational fluid dynamics as a risk assessment tool for aneurysm rupture, Neurosurg. Focus 47 (1) (2019) E12.
[12] J.R. Cebral, et al., Analysis of hemodynamics and wall mechanics at sites of cerebral aneurysm rupture, J. NeuroInterventional Surg. 7 (7) (2015) 530–536.
[13] H. Meng, V. Tutino, J. Xiang, A. Siddiqui, High WSS or low WSS? Complex interactions of hemodynamics with intracranial aneurysm initiation, growth, and rupture: toward a unifying hypothesis, Am. J. Neuroradiol. 35 (7) (2014) 1254–1262.
[14] G. Zhou, Y. Zhu, Y. Yin, M. Su, M. Li, Association of wall shear stress with intracranial aneurysm rupture: systematic review and meta-analysis, Sci. Rep. 7 (1) (2017) 1–8.
[15] L.M. Kadasi, W.C. Dent, A.M. Malek, Colocalization of thin-walled dome regions with low hemodynamic wall shear stress in unruptured cerebral aneurysms, J. Neurosurg. 119 (1) (2013) 172–179.
[16] P. Jiang, et al., Hemodynamic characteristics associated with thinner regions of intracranial aneurysm wall, J. Clin. Neurosci. 67 (2019) 185–190.
[17] J.R. Cebral, X. Duan, B.J. Chung, C. Putman, K. Aziz, A. Robertson, Wall mechanical properties and hemodynamics of unruptured intracranial aneurysms, Am. J. Neuroradiol. 36 (9) (2015) 1695–1703.
[18] N.T. Philip, S. Bolem, B. Sudhir, B. Patnaik, Hemodynamics and bio-mechanics of morphologically distinct saccular intracranial aneurysms at bifurcations: Idealised vs Patient-specific geometries, Comput. Methods Programs Biomed. 227 (2022), 107237.
[19] R. Torii, M. Oshima, T. Kobayashi, K. Takagi, T.E. Tezduyar, Fluid–structure interaction modeling of blood flow and cerebral aneurysm: significance of artery and aneurysm shapes, Comput. Meth. Appl. Mech. Eng. 198 (2009) 3613–3621, 45-46.
[20] K.C. Cho, H. Yang, J.J. Kim, J.H. Oh, Y.B. Kim, Prediction of rupture risk in cerebral aneurysms by comparing clinical cases with fluid–structure interaction analyses, Sci. Rep. 10 (1) (2020) 1–8.
[21] R. Razaghi, H. Biglari, A. Karimi, Risk of rupture of the cerebral aneurysm in relation to traumatic brain injury using a patient-specific fluid-structure interaction model, Comput. Methods Programs Biomed. 176 (2019) 9–16.
[22] A. Vanrossomme, O.F. Eker, J.P. Thiran, G. Courbebaisse, K.Z. Boudjeltia, Intracranial aneurysms: wall motion analysis for prediction of rupture, Am. J. Neuroradiol. 36 (10) (2015) 1796–1802.
[23] J. Zhang, et al., Irregular pulsation of intracranial unruptured aneurysm detected by four-dimensional CT angiography is associated with increased estimated rupture risk and conventional risk factors, J. NeuroInterventional Surg. 13 (9) (2021) 854–859.
[24] J. Zhou, et al., Irregular pulsation of intracranial aneurysm detected by four-dimensional CT angiography and associated with small aneurysm rupture: a single-center prospective analysis, Front. Neurol. 13 (2022), 809286.
[25] M. Hayakawa, et al., CT angiography with electrocardiographically gated reconstruction for visualizing pulsation of intracranial aneurysms: identification of aneurysmal protuberance presumably associated with wall thinning, Am. J. Neuroradiol. 26 (6) (2005) 1366–1369.
[26] E. Oubel, et al., Wall motion estimation in intracranial aneurysms, Physiol. Meas. 31 (9) (2010) 1119.
[27] J.P. Thirion, Image matching as a diffusion process: an analogy with Maxwell's demons, Med. Image Anal. 2 (3) (1998) 243–260.
[28] J. Weickert, A. Bruhn, T. Brox, N. Papenberg, A survey on variational optic flow methods for small displacements. Mathematical Models for Registration and Applications to Medical Imaging, Springer, 2006, pp. 103–136.
[29] S. Balter, D. Ergun, E. Tscholl, F. Buchmann, L. Verhoeven, Digital subtraction angiography: fundamental noise characteristics, Radiology 152 (1) (1984) 195–198.
[30] C. Karmonik, O. Diaz, R. Grossman, R. Klucznik, *In-vivo* quantification of wall motion in cerebral aneurysms from 2D cine phase contrast magnetic resonance images, RöFo Fortschr. Auf Geb. Röntgenstrahlen Bildgeb. Verfahr. 182 (02) (2010) 140–150. © Georg Thieme Verlag KG Stuttgart· New York.
[31] M. Hayakawa, et al., Detection of pulsation in unruptured cerebral aneurysms by ECG-gated 3D-CT angiography (4D-CTA) with 320-row area detector CT (ADCT)

and follow-up evaluation results: assessment based on heart rate at the time of scanning, Clin. Neuroradiol. 24 (2) (2014) 145–150.
[32] F. Lin, Y. Xia, S. Song, N. Ravikumar, A.F. Frangi, High-throughput 3DRA segmentation of brain vasculature and aneurysms using deep learning, Comput. Methods Programs Biomed. 230 (2023), 107355.
[33] T. Hu, et al., Automatic detection of intracranial aneurysms in 3D-DSA based on a Bayesian optimized filter, BioMed. Eng. OnLine 19 (1) (2020) 1–18.
[34] C. Maupu, H. Lebas, Y. Boulaftali, Imaging modalities for intracranial aneurysm: more than meets the eye, Front. Cardiovasc. Med. 9 (2022), 793072.
[35] J. Geng, et al., Advantages of 3D registration technology (3DRT) in clinical application of unruptured intracranial aneurysm follow-up: a novel method to judge aneurysm growth, J. Neuroradiol. 50 (2) (2023) 209–216.
[36] C. Zhang, M. Villa-Uriol, M. De Craene, J. Pozo, A. Frangi, Time-resolved 3D rotational angiography reconstruction: towards cerebral aneurysm pulsatile analysis, Int. J. Comput. Assist. Radiol. Surg 3 (2008) S44–S46.
[37] J. Zhang, et al., Irregular pulsation of aneurysmal wall is associated with symptomatic and ruptured intracranial aneurysms, J. NeuroInterventional Surg. 15 (1) (2023) 91–96.
[38] R. Diab, et al., Advanced cross-sectional imaging of cerebral aneurysms, Br. J. Radiol. 96 (1141) (2023), 20220686.
[39] Y. Peng, R. Khavari, N.A. Nakib, T.B. Boone, Y. Zhang, Assessment of urethral support using MRI-derived computational modeling of the female pelvis, Int. Urogynecology J. 27 (2) (2016) 205–212.
[40] R. Torii, M. Oshima, T. Kobayashi, K. Takagi, T.E. Tezduyar, Fluid–structure interaction modeling of a patient-specific cerebral aneurysm: influence of structural modeling, Comput. Mech. 43 (2008) 151–159.
[41] S. Ji, A. Hartov, D. Roberts, K. Paulsen, Data assimilation using a gradient descent method for estimation of intraoperative brain deformation, Med. Image Anal. 13 (5) (2009) 744–756.
[42] A. Myronenko, X. Song, Point set registration: coherent point drift, IEEE Trans. Pattern Anal. Mach. Intell. 32 (12) (2010) 2262–2275.
[43] H. Wu, J. Wang, J.A.A. Catano, C. Sun, Z. Li, Optical coherence elastography based on inverse compositional Gauss-Newton digital volume correlation with second-order shape function, Opt. Express 30 (23) (2022) 41954–41968.
[44] Y. Cui, et al., Aneurysm morphological prediction of intracranial aneurysm rupture in elderly patients using four-dimensional CT angiography, Clin. Neurol. Neurosurg. 208 (2021), 106877.
[45] H. Xie, J. Song, Y. Zhong, J. Li, C. Gu, K.S. Choi, Extended Kalman filter nonlinear finite element method for nonlinear soft tissue deformation, Comput. Methods Programs Biomed. 200 (2021), 105828.